A New Rotor Structure for High Speed Flywheel Permanent Magnet Synchronous Machine

Zhu, Zichong ; Huang, Yunkai; Dong, Jianning; Peng, Fei

DOI
10.4283/JMAG.2019.24.3.463

Publication date
2019

Document Version
Final published version

Published in
Journal of Magnetics

ISSN (Print) 1226-1750
ISSN (Online) 2233-6656
Journal of Magnetics 24(3), 463-470 (2019) https://doi.org/10.4283/JMAG.2019.24.3.463

A New Rotor Structure for High Speed Flywheel Permanent Magnet Synchronous Machine

Zichong Zhu[1], Yunkai Huang[1]*, Jianning Dong[2], and Fei Peng[1]

[1]*School of Electrical Engineering, Southeast University, Nanjing 210096, China*
[2]*Faculty of Electrical Engineering, Mathematics & Computer Science, Delft University of Technology, Delft 2628CD, The Netherlands*

(Received 21 April 2019, Received in final form 31 July 2019, Accepted 4 August 2019)

This paper presents a new rotor design with assembled permeable retaining sleeve (APRS) to improve performances of a high speed permanent magnet synchronous machine (PMSM). The APRS consists of equal number of permeable and nonmagnetic parts, which are alternately arranged and assembled together circumferentially via keyways. Electromagnetic and mechanical characteristics of the rotor applied to a high speed flywheel PMSM are analyzed using finite element method. Machine performances are compared to an original design with commonly used rotor structure. It shows that phase inductance of the high speed machine increases dramatically due to smaller effective air gap, which may benefit suppressing inverter current harmonics. Also, permanent magnet usage reduces by 9.4 % to obtain identical back electromotive force and torque constant. In addition, a smaller skin depth owing to high-permeability material and the circumferential segmentation of the retaining sleeve effectively reduce rotor eddy current. Associated loss decreases by 40.7 % under open-circuit condition. A prototype rotor is fabricated and preliminary experimental tests are performed to confirm the analysis results.

Keywords : high speed machine, permeable, permanent magnet usage, retaining sleeve, rotor eddy current loss

1. Introduction

High speed permanent magnet synchronous machines (HSPMSMs) become more attractive in applications where high power density and efficiency are essential, such as flywheel energy storage system, air blower and electrically driven system [1, 2]. Due to large flux leakage in rotor bridges and tensile strength limit of silicon steel sheet, the interior permanent magnet machine (IPMM) is less preferable than the surface-mounted permanent magnet machine (SPMM) in high speed applications [3]. Fig. 1 shows common rotor structures in SPMM. Usually, permanent magnets (PMs) are bonded to the rotor hub with nonmagnetic retaining sleeve to fix and protect them from structural failure by large centrifugal force [4].

However, the presence of nonmagnetic component between the stator core and PM lengthens the effective air gap, consequently, increases the reluctance of main magnetic circuit and lowers air gap flux density. As a result, more rare-earth PM and/or armature current are used to compensate it. Also, more rotor eddy current loss is produced when the retaining sleeve is made of metallic material. Special attention should be paid to reducing such loss as the rotor usually has worse heat dissipation capacity than the stator side. Meanwhile, magnetic properties of PM are sensitive to temperature rise.

Moreover, in HSPMSMs, the number of turns in series per phase winding T_{ph} are small due to high fundamental frequency f and limited phase terminal voltage U, given by (1),

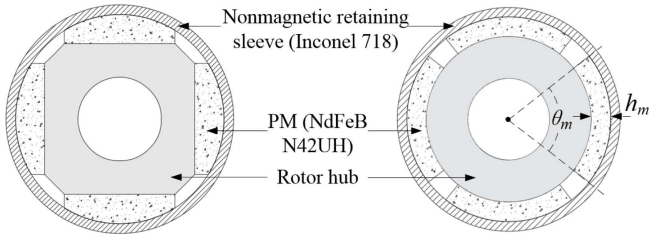

Fig. 1. Commonly used rotor structures for HSPMSM.

*Corresponding author: Tel: +8602583794169
Fax: +8602583791696 e-mail: huangyk@seu.edu.cn

$$U \approx E_{01}=\sqrt{2}\pi f k_{w1} T_{ph} B_{ar1} \frac{D_{air}}{2p} L_{stk} \quad (1)$$

where E_{01}, k_{w1}, p, D_{air}, L_{stk}, B_{ar1} denote back electromotive force (EMF), fundamental winding factor, pole pairs, diameter of air gap, stack length and fundamental component of open-circuit air-gap flux density. Relatively small T_{ph} combining large magnetic circuit reluctance cause extremely small phase inductance of high speed SPMM, compared with low speed machine or IPMM. The small inductance results in more switching harmonics of inverter, which deteriorate control accuracy and induce more stator iron loss, AC copper loss and rotor eddy current loss [5, 6].

Current harmonic suppression methods are derived mainly from the control side, such as using output filter [3], increasing switching frequency [7], and *et al.* These solutions increase system size, capacity requirement of inverter and control algorithm complexity.

New materials for retaining sleeve and novel rotor structures have been developed to increase open-circuit air-gap flux density and machine inductance. A semi-permeable retaining sleeve (50 % cold worked 304L stainless steel, maximum relative permeability μ_{rmax} = 6) is used in [8]. 2 mm thick steel sheets are used to reduce eddy current loss in the retaining sleeve. It shows that the fundamental component of EMF is 20 % higher than the one with magnetically inert retaining sleeve. Fe-20%Cu alloy (μ_{rmax} = 59) and common nonmagnetic materials are comparatively researched in [9], which shows that using semi-permeable material has adverse impact on air-gap flux density and reducing rotor eddy current loss, because part PM flux is "short-circuited" via retaining sleeve.

As for reducing rotor eddy current loss, multilayer sleeve [10], axial segmentation of sleeve and/or magnet [11] and copper cladding [12] are researched. Nevertheless, this measures may cause torque reduction and rotor dynamic problem. New retaining sleeve structures are also proposed. Grooving on titanium alloy retaining sleeve is researched in [13]. Eddy current loss decreases by 23 % with peripheral grooves, whereas axial grooves are less effective and lower rotor strength. A retaining sleeve that looks like skewed cast aluminum cage in induction machine is proposed in [14]. By splitting the current flow path into several smaller ones, the eddy current loss is reduced. Nevertheless, the rotor mechanical integrity is not maintained and eddy current loss in PMs is inevitably increased.

To improve the performances of HSPMSM from above aspects, this paper proposes a novel rotor design to cope with inductance increment, PM usage and rotor eddy current loss reduction. Based on an original machine with commonly used rotor structure, the proposed rotor is applied and its performances are comparatively researched using finite element analysis (FEA). A prototype machine is fabricated. Open-circuit characteristics and static torque are measured to confirm the analysis results.

2. Proposed Rotor Structure

2.1. Original Machine

A 10 kW HSPMSM for flywheel energy storage system is used to evaluate the proposed rotor structure. The original machine has common surface-mounted permanent magnet rotor with nonmagnetic cylindrical sleeve, as shown in Fig. 1 (right) and Fig. 2. 2.5 mm thick retaining sleeve made of high-strength steel Inconel 718 is used to protect PMs from being destroyed during high speed operation. The rotor hub is made of permeable solid steel C45E4 to increase rotor stiffness.

Specifications and design parameters of the original machine are listed in Table 1. Despite doubling the fundamental electrical frequency f when 4-pole rotor is used with respect to a 2-pole one, it helps to increase torque density and reduce the coil pitch thus end winding length of overlapped windings. These features are appreciated in this application that has rigorous axial length limit and short stack length.

2.2. Proposed Rotor Structure

A new rotor with assembled permeable retaining sleeve (APRS) is designed to replace the original rotor in this

Table 1. Design parameters and specifications of the HSPMSM.

Number of poles	4	Number of slots	24
Power (kW)	10	Rotation speed (r/min)	30000
DC bus voltage (V)	380	Rated current (A)	32
Winding layers	2	Coil turns	4
Parallel paths per phase	2	Current density (A/mm^2)	4.5
Physical air gap length (mm)	1.5	Tooth width t_w (mm)	5.3
Stator bore radius r_{si} (mm)	40	Stator external radius r_{so} (mm)	65
Stack length (mm)	60	PM thickness h_m (mm)	7

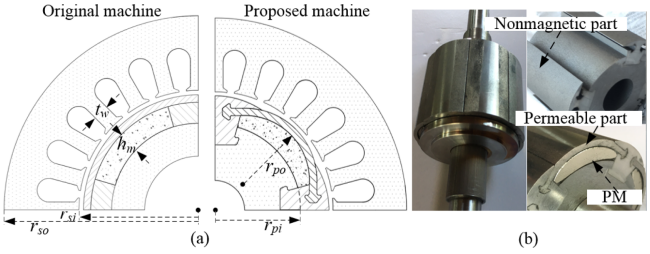

Fig. 2. (Color online) The original and proposed machines. (a) Cross sections. (b) Prototype of the proposed rotor.

machine, as shown in Fig. 2. 4 nonmagnetic and 4 permeable parts are alternately arranged and assembled together via keyways along the circumferential direction. The assembly is connected to the rotor hub though keyways as well. The permeable parts are made of permalloy that has high relative permeability μ_r, high electrical conductivity σ and large saturation flux density B_s, yet low coercive force H_c (μ_r: 54000, H_c: 4.8 A/m, σ: 2.2×10^6 S/m, B_s: 1.5 T). Nonmagnetic parts made of high-strength alloy Inconel 718 in between two permeable parts are designed to reduce inter-pole flux leakage.

For fair comparison, the stator design and physical air-gap length remain unchanged. The thickness of PM h_m is also identical for these two machines, while the outer radius of PM r_{po} in proposed rotor is modified to obtain similar back EMFs. The performances of machines with the original and proposed rotors are comparatively analyzed, involving in back EMF, machine inductance, cogging torque and rotor eddy current loss, as shown in the following section.

3. Performance Improvements

3.1. Open-circuit Performances

The proposed rotor structure reduces the main magnetic circuit reluctance, which may raise the operating point of PM in demagnetization curve though brings more rotor flux leakage, as in Fig. 3. It can be seen that the maximum flux density in stator tooth increases from 1.47 T to 1.62 T due to decreased effective air gap length.

The radial component of open-circuit air-gap flux density B_{ar} in the middle of air gap and their spectra are shown in Fig. 4. To consider the PM flux leakage at the rotor ends, which might be severe in the proposed rotor due to the permeable parts of APRS, 3-D FEA is used to calculate back EMF E_0. Calculated E_0 and its spectrum at 30000 r/min are shown in Fig. 5.

As shown in Fig. 4(a), the peak value of B_{ar} increases from 0.82 T to 0.96 T, which mainly benefits from a

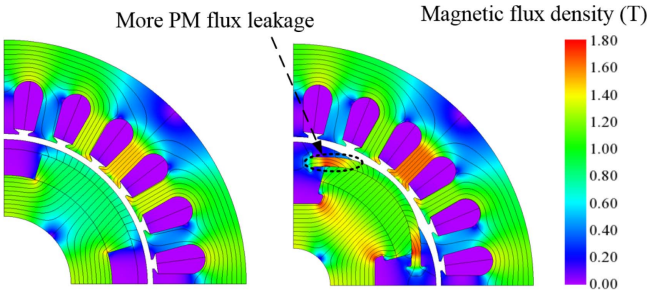

Fig. 3. (Color online) Comparison of open-circuit magnetic field distributions.

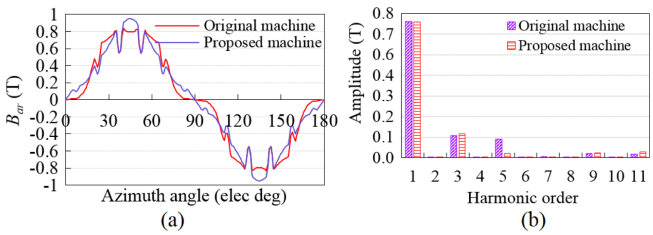

Fig. 4. (Color online) Open-circuit air-gap flux density B_{ar} and its spectrum (20 °C). (a) B_{ar}. (b) Spectra of B_{ar}.

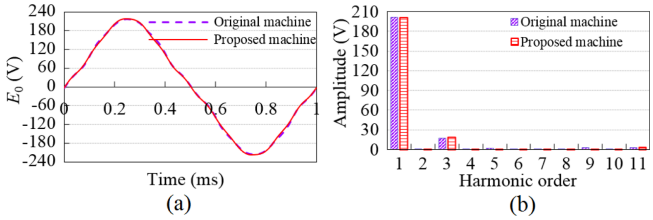

Fig. 5. (Color online) Open-circuit back EMF E_0 and its spectrum. (a) E_0. (b) Spectra of E_0.

smaller effective air gap after introducing the permeable parts of APRS. From Fig. 4(b), the 3rd harmonic of B_{ar} increases slightly compared with the original machine, whereas it does not appear in line back EMF of star connected windings. Most importantly, the troublesome 5th harmonic of B_{ar} decreases considerably that may cause more stator core loss.

The fundamental of open-circuit air-gap flux density of the proposed machine is 0.76 T, which is designed equal to that of the original machine by changing the outer radius of PM, as mentioned above. Therefore, these two machines have similar torque constants and the fundamental component of EMF E_{01}, which are 201.6 V and 200.6 V for the original and proposed machines respectively. Nevertheless, the slightly smaller EMF of the proposed machine are produced with fewer PMs. PM usage M_{pm} decreases by 9.4 % from 0.43 kg to 0.39 kg. The magnetic field establishing ability of PM E_{pm} can be defined as the ratio of E_{01} and PM usage M_{pm}, as in (2). Resultant E_{pm} for original and proposed machines are 468.8 V/kg and 514.4 V/kg respectively. This implies that PM is more effectively used in proposed rotor.

$$E_{pm} = \frac{E_{01}}{M_{pm}} \tag{2}$$

Cogging torque waveforms at open circuit for the original and proposed machines are presented in Fig. 6. The peak-to-peak value of cogging torque decreases from 0.19 Nm to 0.16 Nm when using the new rotor. In other words, albeit downsizing the effective air gap, the introduction of the permeable part of APRS has no obvious

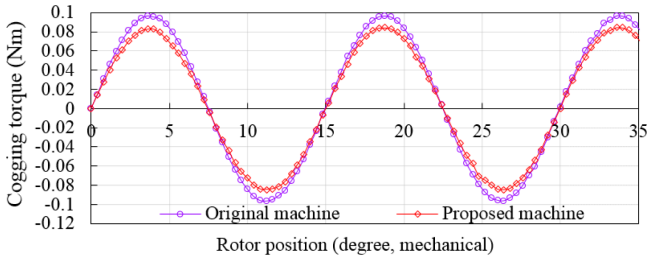

Fig. 6. (Color online) Cogging waveforms of the original and proposed machines by 3D-FEA.

effect on cogging torque.

3.2. Inductance Increment

Machine inductance L is proportional to the square of serial turns per phase winding T_{ph} and reciprocal of the total magnetic circuit reluctance R_n, as in (3). To meet speed requirement with given DC bus voltage, increasing L by using a larger T_{ph} is unavailable. Thus, attention is paid to reducing magnetic circuit reluctance R_n. R_n consists of two components that are in parallel: one is the main magnetic circuit reluctance R_m and another relates to the leakage flux circuit R_σ. Since R_σ is much larger than R_m, L is mainly determined by R_m.

R_m corresponds to armature flux that flows successively through the stator core, air gap, nonmagnetic retaining sleeve, PM and rotor hub, and then returns to the stator core. As the relative permeability of the rotor hub and stator core are high, despite with larger sizes the reluctance of them R_{core}+R_{hub} is still far smaller than that of the air gap R_a, retaining sleeve R_{re} and PM R_{pm}. As a result, R_m is approximately equal to R_a+R_{re}+R_{pm}, given by (4).

$$L \propto \frac{T_{ph}^2}{R_n} = \frac{(R_m + R_\sigma)T_{ph}^2}{R_m R_\sigma} = \frac{T_{ph}^2}{R_m} \tag{3}$$

$$L \propto \frac{T_{ph}^2}{R_m} = \frac{T_{ph}^2}{R_{core} + R_{hub} + R_a + R_{re} + R_{pm}} \approx \frac{T_{ph}^2}{R_a + R_{re} + R_{pm}} \tag{4}$$

The proposed rotor replaces the nonmagnetic retaining sleeve in the original rotor with a permeable one, which drastically reduces R_{re} and thus R_m. Consequently, phase inductance L is increased. Magnetic field distributions with only d- or q-axis current of the original and proposed machines are shown in Fig. 7 (assuming that PMs are not magnetized).

As in Fig. 7(a), the q-axis flux goes through the air gap, nonmagnetic retaining sleeve, PM, rotor hub and then returns to the stator core. Whereas in the proposed rotor,

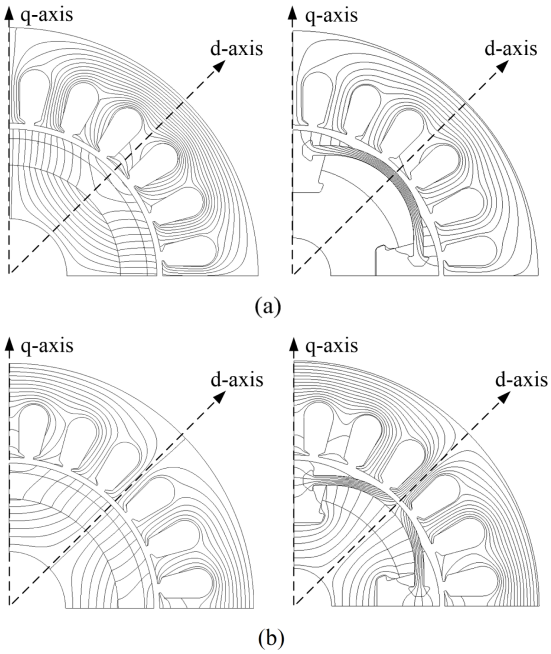

Fig. 7. Magnetic field distributions. (a) i_q = 45 A, i_d = 0 A. (b) i_q = 0 A, i_d = 45 A.

an extra flow path for q-axis flux is provided by the permeable part of APRS, which "short-circuits" the PM and rotor hub. This reduces the reluctance of q-axis magnetic circuit.

As for d-axis magnetic circuit in Fig. 7(b), the flow path of d-axis flux is nearly the same as that of q-axis flux in the original machine, which presents a non-salient behavior. Nevertheless, flow paths of d- and q-axis fluxes are different in the new rotor. As mentioned above, PM and rotor hub are bypassed for q-axis flux, whereas part of d-axis flux still crosses PM and enters the rotor hub, as shown in Fig. 7(b). As a result, the reluctance of d-axis magnetic circuit is larger compared with that of q-axis in

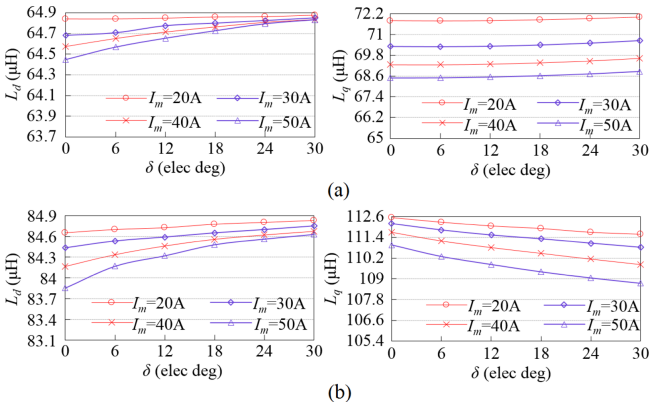

Fig. 8. (Color online) Inductances against various current phase advance angles and amplitudes. (a) Original machine. (b) Proposed machine.

the new rotor. Conversely, q-axis inductance L_q is larger than d-axis inductance L_d. That is, the proposed rotor shows magnetic saliency.

The inductance of q- and d-axis at different current amplitudes I_m and phase advance angles δ are calculated with FEA, as shown in Fig. 8. Average d-axis inductance increases by 31.7 % from 64.6 μH to 85.3 μH. For q-axis inductance, the increment is 58.4 %, from 70.1 μH to 111.0 μH. It is noteworthy that there is obvious difference between L_d and L_q in the proposed machine, therefore, a large saliency ratio is obtained. In addition, L_q of the proposed machine decreases when increasing δ. The reason is that q-axis circuit becomes more saturated with larger d-axis current.

3.3. Rotor Eddy Current Loss Reduction

Rotor eddy current loss in retaining sleeve and PMs are mainly resulted from the spatial harmonics of armature magnetomotive force (MMF) and the permeance harmonics. The proposed APRS consists of several electrically insulated parts along the circumferential direction, which hinder cylindrical eddy current flows and effectively reduce associated loss. On the other hand, the permeable part of APRS is made of permalloy that features high

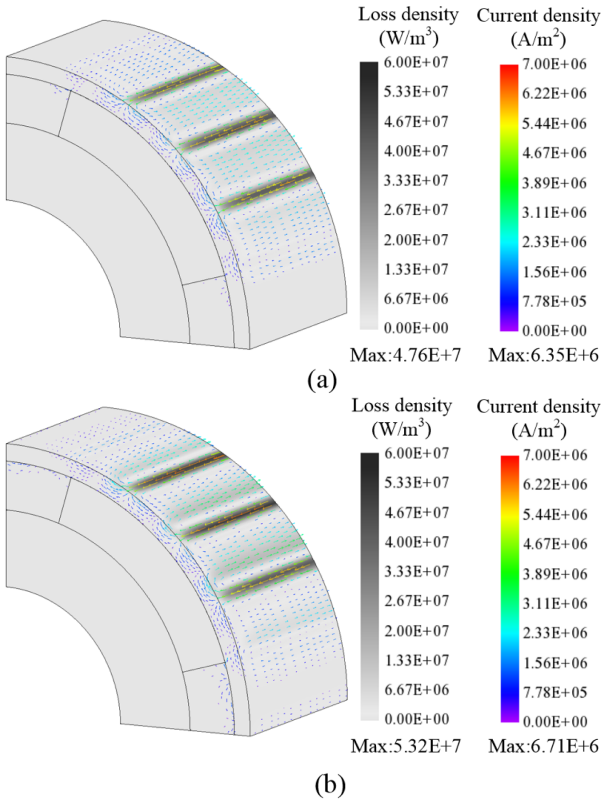

Fig. 9. (Color online) Rotor eddy current and associated loss distributions of the original machine. (a) Open circuit (30000 r/min). (b) Rated operating point (30000 r/min, 10 kW).

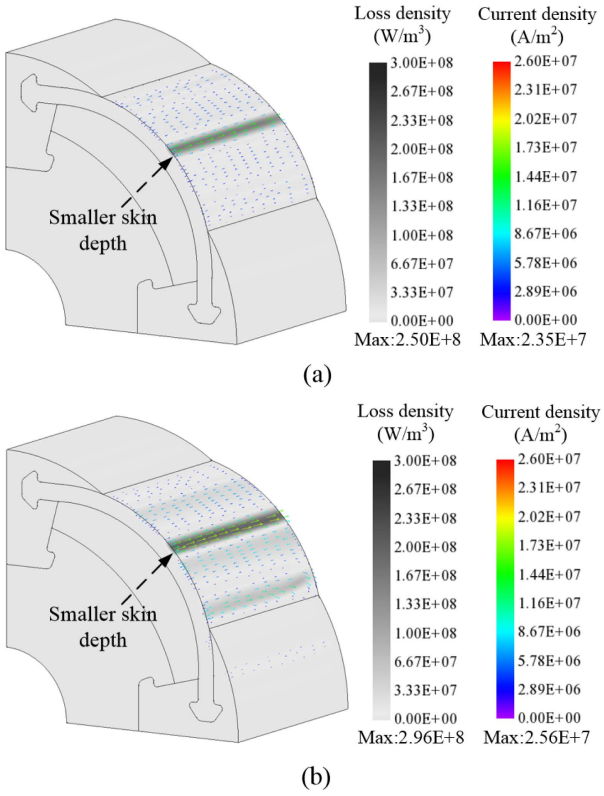

Fig. 10. (Color online) Rotor eddy current and associated loss distributions of the proposed machine. (a) Open circuit (30000 r/min). (b) Rated operating point (30000 r/min, 10 kW).

relative permeability, high electrical conductivity and low coercive force. Hysteresis loss in the permeable parts of APRS produced by asynchronous harmonics is negligible compared with eddy current loss. For example, the hysteresis loss at rated operating point is only 4.67 W, while eddy current loss is 59.8 W.

The distribution of rotor eddy current and associated loss at open circuit and on-load operating point are calculated by 3-D FEA, and are presented in Fig. 9 and Fig. 10. It can be seen that a smaller skin depth δ_{sk} is produced due to the higher relative permeability μ_r and electrical conductivity σ of permalloy Supra 50 than non-magnetic alloy Inconel 718, as in (5), where f is the frequency of the asynchronous harmonic.

$$\delta_{sk} = \sqrt{1/\pi f \mu_r \mu_0 \sigma} \tag{5}$$

For the 6th harmonic (f = 6000 Hz), the skin depth is 0.02 mm for permeable part of APRS, which means that PMs and rotor hub have nearly no eddy current loss due to the "shielding effect". This "shielding effect" is realized by wrapping metallic nonmagnetic retaining sleeve with high-conductivity copper cladding in [12], whereas in the new rotor it results from high-permeability material. Also,

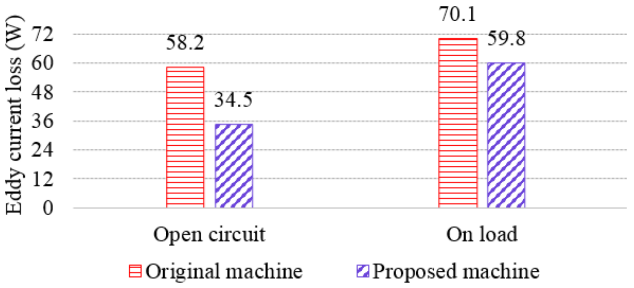

Fig. 11. (Color online) Rotor eddy current loss calculated using 3-D FEA for the original and proposed machines.

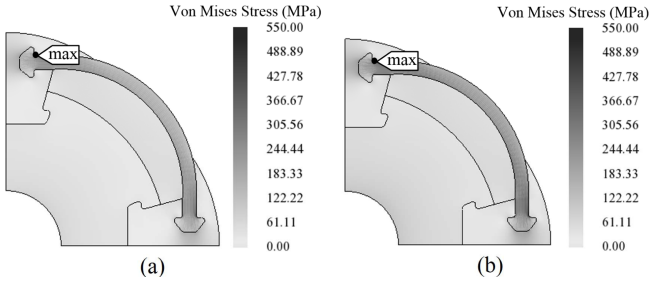

Fig. 12. Von Mises stress distributions in proposed rotor. (a) 30000 r/min. (b) 36000 r/min.

using permeable material makes better use of permanent magnet, as mentioned in Part 3.1, which is unavailable with copper cladding.

Comparatively, the maximum eddy current and associated loss densities are increased in proposed rotor. For example, at open circuit, rotor eddy current density increases from 6.35×10^6 A/m^2 to 2.35×10^7 A/m^2, while associated loss density increases from 4.76×10^7 W/m^3 to 2.50×10^8 W/m^3. However, rotor eddy current distribution is dramatically narrowed due to circumferential segmentation and a smaller skin depth. As a result, the total rotor eddy current loss are significantly decreased, particularly at open circuit, as shown in Fig. 11. Rotor eddy current loss decreases by 40.7 % from 58.2 W to 34.5 W at open circuit. Since the rotor is installed in a high vacuum chamber to eliminate windage loss, heat dissipation from rotor surfaces to the air gap by thermal convection is unavailable. Rotor eddy current loss can only be dissipated via shaft by thermal conduction. Therefore, rotor eddy current loss reduction is vital for lowering rotor temperature rise.

Certainly, commonly used axial segmentation of retaining sleeve [11] can also be used to further suppress rotor eddy current. For example, by dividing each part of APRS into two individual parts axially, the open-circuit rotor eddy current loss decreases 0.8 W. This method is more effective for the original rotor as the decrement is 7.25 W with two axial segments. Accordingly, axial segmentation is not used in prototype considering rotor stiffness and manufacturing complexity.

4. Rotor Integrity Evaluation

The rotor hub of the original and proposed machines are made of permeable solid steel rather than silicon steel sheet lamination. High rotor rigidity is well kept and the maximum operation speed is far below the 1st order critical speed. Thus structural analysis focuses on rotor integrity evaluation as replacing integral retaining sleeve with an assembled one may cause structural strength failure.

The Von Mises stress distributions at 30000 r/min, steady state temperature (from thermal FE analysis) and 36000 r/min are displayed in Fig. 12. Centrifugal force and thermal stress due to thermal expansion are considered. Electromagnetic nodal force on each part is small and neglected compared with the above two sources.

It can be seen that the maximum Von Mises stress in the permeable part locates at the fillet of keyway and reaches 509.0 MPa, 552.1 MPa at 30000 r/min, 36000 r/min respectively. These values are under the allowable stress of Supra50 which has a yield strength 820 MPa. For nonmagnetic part, nickel-chromium based alloy Inconel 718 has a yield strength more than 1000 MPa. The maximum Mises stress in it is also in permitted range.

Permanent magnets are usually considered as brittle materials. For sintered magnet N42UH used in the prototype, it has high compressive strength 1100 MPa, but low tensile strength 73.5 MPa. Pretensions are not used in the proposed rotor as PMs are constrained both radially and circumferentially by APRS. Thermal expansion coefficient difference between the permeable part of APRS and the rotor hub keeps PM compressed. The maximum and minimum principal stresses in PM are 34.7 MPa and 123.0 MPa, which are under allowable values of the tensile and compressive strengths with a safety factor 2.0.

Rotor deformations under these two operating points

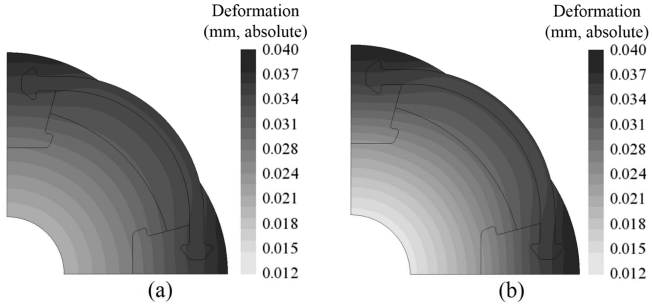

Fig. 13. Rotor deformations of the proposed machine. (a) 30000 r/min. (b) 36000 r/min.

are shown in Fig. 13. The maximum deformations are 0.034 mm and 0.039 mm on the outside edge of non-magnetic part of APRS. It can also be seen that PMs are always compressed at this two operating points.

5. Experimental Tests

A prototype rotor is fabricated to confirm the analysis results, as shown in Fig. 2. Experimental setups are constructed to measure machine parameters and perform some preliminary tests. Back EMFs are measured when the prototype is driven by another high speed PM machine, as in Fig. 14(a). Measured and calculated EMF waveforms at 30000 r/min are shown in Fig. 15. The amplitude of calculated and measured EMFs are 217.9 V and 223.1 V respectively. It can be seen that the 3-D FEA results show good agreement with the measured values.

As shown in Fig. 8, d-axis inductance L_d is not equal to q-axis inductance L_q, i.e., synchronous inductance L_s depends on rotor position θ and the proposed rotor shows salient behavior. To confirm these results, L_s is measured at various rotor positions that are determined by a dividing head (θ equals to 0 when the rotor d-axis is aligned with the axis of phase winding), as in Fig. 14(b). Measured and calculated phase inductances are plotted in Fig. 16. It can be seen that phase inductance varies with rotor position, that is, L_d is not equal to L_q. Meanwhile, measured inductances are slightly larger than that from FEA, which

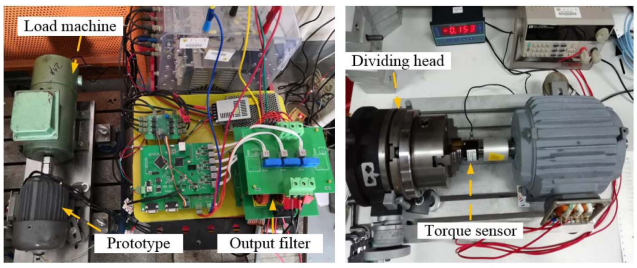

Fig. 14. (Color online) Experimental setups for measuring back EMFs, machine parameters and static torques.

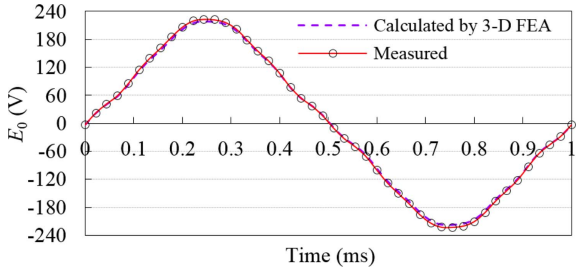

Fig. 15. (Color online) Measured and calculated open-circuit EMFs at 30000 r/min.

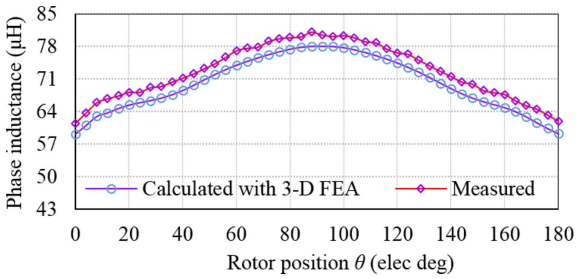

Fig. 16. (Color online) Measured and calculated phase inductances against rotor positions.

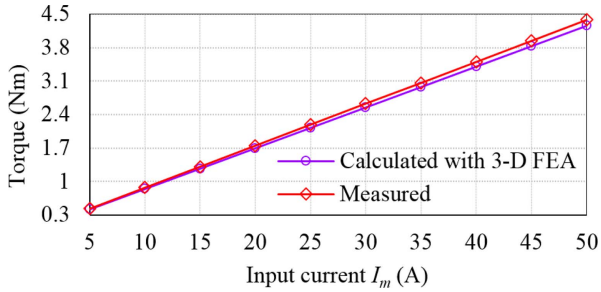

Fig. 17. (Color online) Output torques with various input currents.

Table 2. Result comparisons between FEA and experiment.

Parameters	3D-FEA	Experiment	Error (%)
The constant of phase EMF (Vs/rad)	0.069	0.071	2.41
Torque constant (Nm/A)	0.0847	0.0873	2.98
D-axis inductance (μH)	88.87	92.23	3.64
Q-axis inductance (μH)	117.0	121.72	3.88

may result from a larger end winding inductance since the end winding length in prototype is larger than the predicted value in FEA.

Fig. 17 presents calculated and measured static torques at various current amplitudes with high precision torque transducer, as shown in Fig. 14(b). It can be seen that calculated and measured results show excellent consistency, the maximum difference is only 3.26 %. Measured torques are slightly larger than calculated values, which may result from better PM magnetic properties since measured EMFs are also slightly larger than calculated results. The comparison between the analysis and experiment results is summarized in Table 2. The maximum error is only 3.88 %, which confirms the accuracy of FEA and the advantages of the proposed rotor.

6. Conclusion

A new rotor structure with assembled permeable retaining sleeve is proposed in this paper to improve performances

of high speed surface-mounted permanent magnet synchronous machine. Due to the decreased magnetic circuit reluctance, the q- and d-axis inductances are both increased compared with the original machine. Meanwhile, with smaller effective air gap, rare-earth PM usage is reduced to obtain similar air-gap flux densities and back EMFs. In addition, proposed APRS contains several mutually insulated parts, which effectively suppresses eddy current flows along the circumferential direction. On the other hand, the permeable part of APRS has high permeability and electrical conductivity, thus produce a small skin depth. These two reasons contribute to an obvious rotor eddy current loss reduction. Prototype machine is fabricated and preliminary test results show good agreement with calculated values.

Acknowledgement

This work was supported in part by the Natural Science Foundation of China (51777034).

References

[1] S. H. Lee, Y. J. Kim, K. S. Lee, and S. J. Kim, J. Magn. **20**, 444 (2015).
[2] J. H. Park, K. S. Lee, S. H. Lee, and S. Y. Jung, J. Magn. **22**, 430 (2017).
[3] N. Uzhegov, A. Smirnov, C. H. Park, J. H. Ahn, J. Heikkinen, and J. Pyrhönen, IEEE Trans. Ind. Electron. **64**, 8427 (2017).
[4] A. Binder, T. Schneider, and M. Klohr, IEEE Trans. Ind. Appl. **42**, 1031 (2006).
[5] S. Li, Y. Li, W. Choi, and B. Sarlioglu, IEEE Trans. Transp. Electrification. **2**, 2 (2016).
[6] R. R. Moghaddam, 2014 IEEE Energy Conversion Congress and Exposition (ECCE). 5539 (2014).
[7] Z. Chen, Y. Yao, D. Boroyevich, K. D. T. Ngo, P. Mattavelli, and K. Rajashekara, IEEE Trans. Power Electron. **29**, 2307 (2014).
[8] J. M. Yon, P. H. Mellor, R. Wrobel, J. D. Booker, and S. G. Burrow, IEEE Trans. Energy Convers. **27**, 646 (2012).
[9] W. Li, H. Qiu, X. Zhang, J. Cao, S. Zhang, and R. Yi, IEEE Trans. Ind. Electron. **61**, 3030 (2014).
[10] H. Fang, R. Qu, J. Li, P. Zheng, and X. Fan, IEEE Trans. Ind. Appl. **53**, 3411 (2017).
[11] M. Mirzaei, A. Binder, B. Funieru, and M. Susic, IEEE Trans. Magn. **48**, 4831 (2012).
[12] M. R. Shah and A. M. EL-Refaie, IEEE Trans. Ind. Appl. **45**, 720 (2009).
[13] J. X. Shen, H. Hao, M. J. Jin, and C. Yuan, IEEE Trans. Magn. **49**, 3973 (2013).
[14] H. W. Jun, J. Lee, H. W. Lee, and W. H. Kim, IEEE Trans. Magn. **51**, 1 (2015).
[15] T. A. Huynh and M. Hsieh, IEEE Trans. Magn. **53**, 1 (2017).